Evolution of noncollinear magnetism in magnetocaloric MnPtGa

Joya A. Cooley,[1,*] Joshua D. Bocarsly,[1,2] Emily C. Schueller,[1,2] Emily E. Levin,[1,2] Efrain E. Rodriguez,[3] Ashfia Huq,[4] Saul H. Lapidus,[5] Stephen D. Wilson,[2] and Ram Seshadri[1,2,6]

[1]*Materials Research Laboratory, University of California, Santa Barbara, Santa Barbara, California 93106, USA*
[2]*Materials Department, University of California, Santa Barbara, Santa Barbara, California 93106, USA*
[3]*Department of Chemistry and Biochemistry, University of Maryland, College Park, Maryland 20742, USA*
[4]*Neutron Scattering Division, Oak Ridge National Laboratory, Oak Ridge, Tennessee 37831, USA*
[5]*X-ray Sciences Division, Argonne National Laboratory, Lemont, Illinois 60439, USA*
[6]*Department of Chemistry and Biochemistry, University of California, Santa Barbara, Santa Barbara, California 93106, USA*

(Received 6 July 2019; revised manuscript received 18 February 2020; accepted 17 March 2020; published 13 April 2020)

MnPtGa crystallizes in the hexagonal Ni_2In structure type in space group $P6_3/mmc$ and has been reported to display a ferromagnetic Curie temperature near 220K. Here we find a transition near $T_C = 236$ K to a ferromagnetic state, albeit with a reduced moment from what is expected for collinear ordering. The peak magnetocaloric entropy change was determined to be $\Delta S_M = -1.9\,\mathrm{J\,kg^{-1}\,K^{-1}}$ for an applied magnetic field of $H = 5$ T at the ferromagnetic ordering temperature. Magnetostructural coupling manifests as a change in the slope of the thermal expansion coefficients of the c lattice parameter near T_C, with a negative spontaneous volume magnetostriction; $\omega = -300$ ppm at 190K. Neutron powder diffraction studies of the magnetic ground state reveal an evolution in complexity as temperature decreases: from a ferromagnet, to a canted antiferromagnet, to the eventual formation of a spin-density-wave state at low temperatures.

DOI: 10.1103/PhysRevMaterials.4.044405

I. INTRODUCTION

Magnetic materials containing 5*d* transition elements are often found to have a richness of observed properties. In addition to the potential for magnetic hardening associated with the strong spin-orbit coupling effects of the later 5*d* elements [1,2], these compounds can display invar effects [3,4], complex magnetostructural behavior [5], and the potential for hosting magnetic Weyl fermions [6]. In this regard, we have closely investigated MnPtGa, which thus far is a not-very-well-studied compound of the Ni_2In structure type, first described by Buschow *et al.* in 1983 [7]. The compound is reported to be ferromagnetic near 220 K and to crystallize in the hexagonal Ni_2In structure type in space group $P6_3/mmc$. Furthermore, this material has recently been suggested as possessing a broken center of inversion symmetry, which allows it to display thermodynamically stable Neél-type skyrmions between around 210 and 220 K and metastable skyrmions in a much broader temperature range, down to at least 5 K [8].

It has been suggested that promising candidate materials for magnetic refrigeration via the magnetocaloric effect can be evaluated through a computational proxy known as magnetic deformation, or Σ_M [9,10]. This proxy is a predictor of the strength of magnetostructural coupling in a given material calculated using density functional theory (DFT). When DFT-based structural optimizations are performed with and without spin polarization, the difference between the two relaxed structures can be quantified as Σ_M, in which a high value is found to correspond with a strong magnetocaloric effect. The calculated Σ_M can be correlated with magnetocaloric properties even in materials where the magnetic transition is not coupled to a structural phase transition [11]. Through this proxy, MnPtGa emerged as a candidate meriting experimental study for high magnetocaloric performance. Magnetic deformation calculations of MnPtGa showed $\Sigma_M = 2.4\%$, and prior findings have classified $\Sigma_M > 1.5\%$ as promising.

Upon preparing and studying MnPtGa, however, we found that its magnetic properties, including its magnetization vs temperature, saturated moment, and magnetocaloric effect, were inconsistent with those of a simple collinear ferromagnet, as it has been reported to be. This motivated us to use neutron powder diffraction (NPD) and DFT to understand the evolution of the magnetic structure below T_C.

Here we present a detailed structural and magnetic characterization of MnPtGa using magnetic measurements, synchrotron and neutron powder diffraction, and density functional theory calculations. Our samples adopt a hexagonal Ni_2In-type nuclear structure and exhibit a complex temperature evolution of magnetic structure, including ferromagnetic and canted antiferromagnetic phases and a canted spin-density-wave ground state. Temperature-dependent synchrotron diffraction reveals that these magnetic phase transitions are coupled magnetoelastically to the lattice parameters. These rich magnetic states are also expected to impact the formation and behavior of skyrmions and other long-wavelength chiral magnetic states.

*jacooley@mrl.ucsb.edu

II. MATERIALS AND METHODS

Polycrystalline ingots of MnPtGa were prepared using a combination of arc melting and furnace annealing. Elemental Mn (99.95%; Alfa Aesar) was cleaned before use by annealing it overnight sealed in an evacuated fused silica tube at 1273 K. Purified Mn was then ground and combined with Pt powder (99.9%; Strem) and pieces of Ga buttons (Alfa Aesar; 99.9999%) totaling about 0.5 g (or 1.5 g, for neutron diffraction samples). Excess Mn (10 at%) was added to account for Mn loss during heating. Preweighed Mn and Pt powders were pelletized into 6-mm pellets, then arc-melted with Ga in an Ar atmosphere, turned over, and melted again for homogeneity. The resultant ingot was wrapped in Ta foil, sealed in an evacuated fused silica ampoule (approx. 8-cm length, 9.5-mm I.D.), and annealed for 6 days at 1073 K. The furnace was turned off and allowed to cool to room temperature.

Neutron powder diffraction data were collected at 300, 200, 150, 50, and 10 K at the POWGEN diffractometer [12] at the Spallation Neutron Source at Oak Ridge National Laboratory on 1.5 g of polycrystalline powder. Patterns at all temperatures were collected using a center wavelength of the neutron packet of 2.665 Å, and additional patterns using a center wavelength of 0.8 Å were collected at 300 and 10 K. The longer-wavelength data provide an extremely high resolution and sensitivity at low Q, while the shorter-wavelength data provide a much larger Q range. The magnetic structure supercells were determined with the aid of the K-Search program included with FullProf Suite [13] and the magnetic structures were solved with the aid of ISODISTORT [14,15] and TOPAS Academic V6 [16]. Representations of the nuclear and magnetic structures were drawn with VESTA-3 [17]. Atomic displacement parameters (B_{eq}) were determined at 300 and 10 K from corefinement of data from center wavelengths of 2.665 and 0.8 Å. For the intermediate temperatures, only data for a center wavelength of 2.665 Å were available and therefore B_{eq} values were fixed to values linearly interpolated between the 300 and the 10 K data to reduce correlations.

Temperature-dependent synchrotron powder x-ray diffraction data were collected using the area detector on beamline 11-BM at the Advanced Photon Source, Argonne National Laboratory ($\lambda \approx 0.4$ Å). Due to the high x-ray absorption of Pt at this wavelength, the powder was adhered to the outside of a 1.1-mm-I.D. Kapton capillary with a small amount of vacuum grease. The sample was cooled from 280 to 180 K using a nitrogen cryostream at a rate of 0.4 K min^{-1}. Ten-minute scans were taken, resulting in each scan averaging over 4 K using $\lambda = 0.412825$ Å. For further analysis, additional measurements were taken with a two-dimensional area detector in which the sample was cooled from 300 to 100 K at a rate of 5 K min^{-1} using a nitrogen cryostream. During the cooling, a diffraction image was taken every 20 s using $\lambda = 0.457845$ Å). The two-dimensional images were integrated using GSAS-II [18], and the patterns were refined sequentially using TOPAS Academic V6.

The possibility of compositional inhomogeneity in MnPtGa was examined using an FEI Apreo C scanning electron microscope. A piece from the arc-melted ingot was mounted in epoxy, ground using SiC paper, and then polished down to 0.25 μm using diamond suspension. Images were acquired at an accelerating voltage of 5 keV using a backscattered electron detector, which provides both electron density contrast and orientation contrast. For composition analysis, sample powder was blended with $\approx$ 10 wt% SPEX 3646 paraffin binder and pelletized into a 6-mm disk, and five points across the pellet surface were analyzed with a Rigaku ZSX Primus VI wavelength dispersive x-ray fluorescence instrument using a 0.5-mm spot size.

Magnetic properties were measured on 6 to 10 mg of powder ground from an annealed ingot in a Quantum Design MPMS3 equipped with a vibrating sample magnetometer. For zero-field-cooled (ZFC) and field-cooled (FC) measurements, magnetization (M) vs temperature (T) data were acquired upon warming at a rate of 7 K min^{-1}. An Arrott plot was constructed with one quadrant M vs applied field (H) measurements (i.e., 0 to 5 T) at 3-K intervals between 170 and 260 K. In order to determine ΔS_M, M vs T measurements were taken upon cooling at various fields from $H = 0.1$ T to $H = 5$ T. The temperature dependence of ΔS_M for a magnetic field change of 0 to 5 T was derived from isothermal magnetization curves using the Maxwell relation,

$$\left(\frac{\partial S}{\partial H}\right)_T = \left(\frac{\partial M}{\partial T}\right)_H, \tag{1}$$

which relates the slope of magnetization vs temperature to the slope of entropy (S) vs field. The field-driven isothermal entropy change ΔS_M can then be calculated using

$$\Delta S_M(H,T) = \int_0^H \left(\frac{\partial M}{\partial T}\right)_{H'} dH'. \tag{2}$$

Temperature derivatives of the $M(T)$ traces were calculated using Tikhonov regularization [19], and then integrals with field were calculated using the trapezoid method to obtain ΔS_M. This procedure was carried out using the MAGENTRO.PY code [20].

Electronic structure calculations were performed using density functional theory, as implemented in the Vienna Ab initio Simulation Package [21] with projector-augmented-wave pseudopotentials [22,23] within the Perdew-Burke-Ernzerhof generalized gradient approximation [24]. First, the hexagonal unit cell of MnPtGa was relaxed in non-spin-polarized and spin-polarized calculations with a force convergence of 0.001 eV Å^{-1} and no spin-orbit coupling included. The spin-polarized calculation was then initialized with a starting ferromagnetic moment of 3 μ_B per Mn. Densities of states with and without spin polarization were obtained from static calculations on these structures using a $10 \times 10 \times 8$ Γ-centered k-point grid and an energy convergence criterion of 10^{-5} eV. Calculations including spin-orbit interactions were performed under the same conditions, starting with collinear ferromagnetic spin structures with the spins aligned in either the [100] or the [001] direction. In addition, a constrained moment calculation was performed to simulate the canted antiferromagnetic structure. In this calculation, an energy penalty was used to constrain the moments to angles of 22° from the [001] direction with no constraint on moment magnitudes.

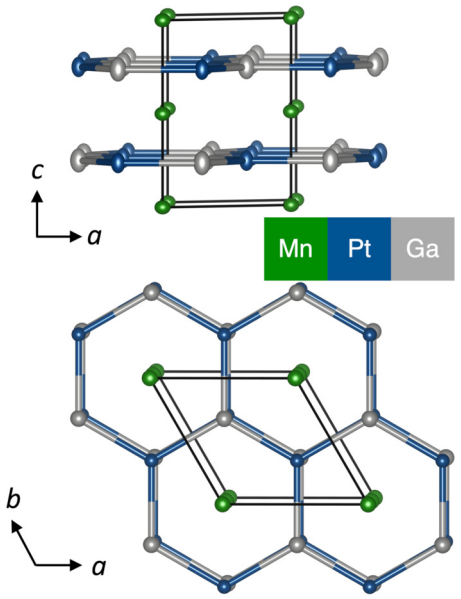

FIG. 1. Two views of the MnPtGa crystal structure, with atoms represented using displacement ellipsoids shown at 95% probability. The structure is viewed down the b axis to emphasize how Pt-Ga layers alternate with Mn layers and down the c axis to emphasize the honeycomb Pt-Ga lattice.

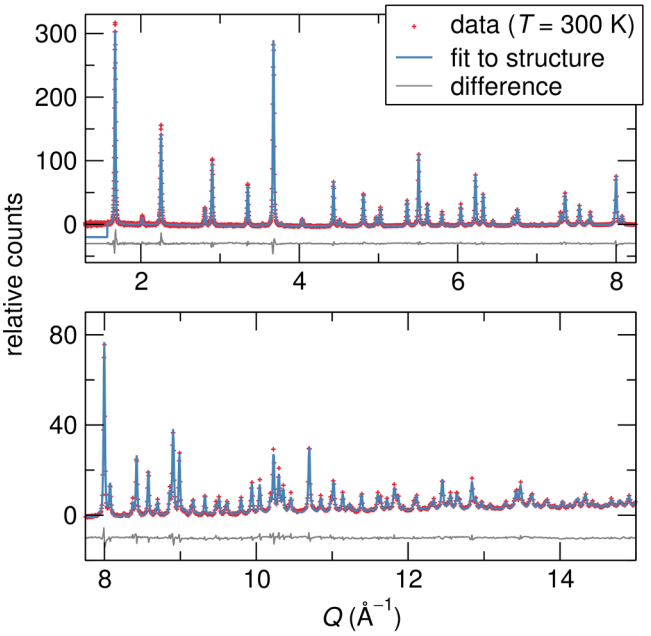

FIG. 2. Rietveld refinement results of the $T = 300$ K neutron powder diffraction data fit to the structure in the $P6_3/mmc$ space group, revealing a single-phase sample fit with a high certainty. For greater clarity, the fits are shown separately for lower and higher Q values in the upper and lower panels. In both panels, the difference has been offset.

III. RESULTS AND DISCUSSION

A. Structural characterization

MnPtGa has been previously reported to form in the hexagonal Ni_2In structure type (space group $P6_3/mmc$; No. 194) [25], as depicted in Fig. 1. The structure can be visualized as a honeycomb lattice of Pt and Ga atoms (in the 2c and 2d Wyckoff sites, respectively). These atoms are connected in the ab plane and stacked along the c axis in alternating ($ABAB$) slabs offset in the ab plane by $\frac{1}{3}$ of the unit cell. The PtGa slabs are stuffed with Mn (site 2a) ordered on a hexagonal lattice.

A recent report by Srivastava *et al.* [8] showed the formation of Néel-type skyrmions in a single-crystal sample of MnPtGa. The stabilization of magnetic skyrmions implies a crystal structure with a noncentrosymmetric space group, which is in agreement with their finding of the polar space group $P3m1$ (No. 156) for their crystals rather than the previously reported centrosymmetric $P6_3/mmc$ structure. The $P3m1$ structure differs from the $P6_3/mmc$ by a symmetry-breaking corrugation of the Pt-Ga honeycomb layers. Srivastava *et al.* present single-crystal x-ray diffraction data that clearly show the presence of weak peaks which are forbidden by $P6_3/mmc$ extinction rules but are allowed in $P3m1$, namely, $(00l)$, with $l = 2n + 1$. However, we see no evidence of these space-group violations in our samples using synchrotron x-ray diffraction and NPD at temperatures between 10 and 300 K. Given the resolution and sensitivity of the diffraction instrumentation utilized in this work, we would expect to be able to easily resolve the weak peaks arising from the structure reported by Srivastava *et al.*, as demonstrated in the Supplemental Material [26], Figs. S1 and S2. Therefore, we conclude that differences in sample preparation for the powder samples in this study vs the Bridgeman-grown single-crystal samples in the Srivastava *et al.* report evidently lead to slightly different crystal structures. However, we note that the Mn sublattice in both crystal structures is the same; therefore, we expect that magnetic structures similar to those we report for our samples are likely to form in samples with the distorted crystal structure. Further research is clearly called for in order to determine how subtle compositional and preparation details can be used to control the structural (and therefore skyrmionic) properties of MnPtGa.

Room-temperature NPD data are shown in Fig. 2 along with a structural Rietveld refinement to the $P6_3/mmc$ structure type. The fit to the data shows that the sample is single phase, with all observed peaks matching the model. When refining the site occupancy at each site, the Pt site is found to contain approximately 1.50(4)% Mn, while the Mn and Ga sites are fully occupied with their respective atoms and do not appear to contain mixed occupancy of other atoms (within the resolution of the instrument). Refined lattice parameters [$a =$ 4.3313(3) Å, $c = 5.5738(6)$ Å] are within 1% of both the room-temperature parameters provided in a previous report on $P6_3/mmc$ [25].

The large Q-space range of the POWGEN data with center wavelength 0.8 Å (Supplemental Material, Fig. S4) allows for the accurate refinement of anisotropic atomic displacement parameters, which are shown as 95% ellipsoids in Fig. 1. While the Mn atom motion is relatively spherical, the Pt and Ga atomic displacement parameters are much more anisotropic, with more vibration occurring perpendicular to the basal plane at room temperature. As expected, the heavier Pt atoms have smaller displacements than the Ga atoms.

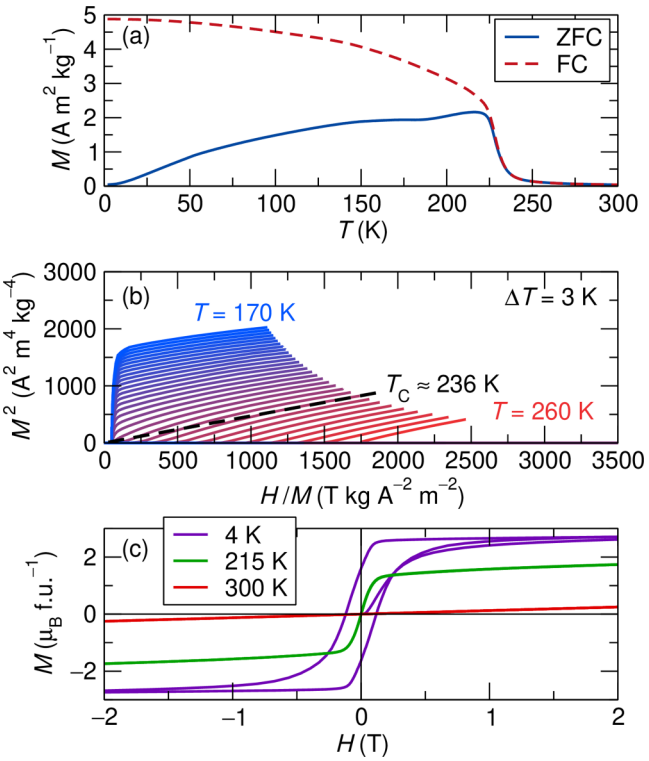

FIG. 3. (a) Temperature–dependent zero-field-cooled (ZFC) and field-cooled (FC) magnetization measurements of MnPtGa measured under an $H = 20$ mT field reveal complex magnetic behavior with T_C near 230 K and additional ordering near 200 K in the ZFC trace and near 150 K in the FC trace. (b) Isothermal field-dependent magnetization measurements are plotted in the Arrott style to emphasize the true T_C near 236 K. (c) Field–dependent magnetization measurements at 300, 215, and 4 K reveal that both M_{sat} and coercivity increase with decreasing temperature.

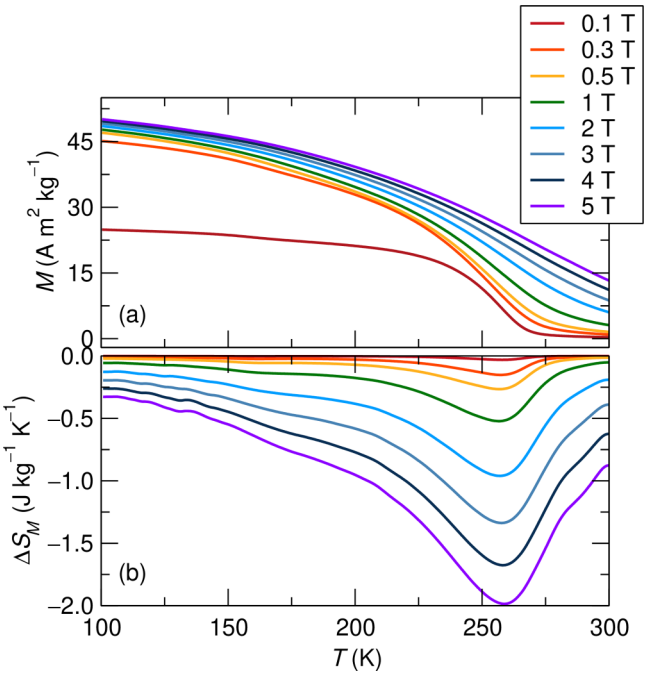

FIG. 4. (a) Temperature–dependent magnetization is measured at select fields to calculate ΔS_M. (b) Derivatives of each curve are calculated and integrated according to Eq. (2), yielding ΔS_M.

The phase purity of the sample was further confirmed using backscattered electron microscopy (Fig. S3, Supplemental Material). X-ray fluorescence analysis revealed an average composition of $Mn_{1.067(3)}Pt_{0.978(3)}Ga_{0.956(5)}$, suggesting a slight excess of Mn. Further details of the x-ray fluorescence analysis can be found in the Supplemental Material, Table S1.

B. Magnetic property characterization

Figure 3(a) displays the temperature-dependent magnetization of MnPtGa between 2 and 300 K under an applied field (H) of 20 mT. Both zero-field-cooled and field–cooled data are shown. Below the ordering temperature of approximately 230 K, clear thermomagnetic irreversibility is observed between the ZFC and the FC measurements. In addition, kinks in the magnetization below the Curie temperature in both the ZFC (near 200 K) and the FC (near 150 K) curves can be seen, which suggests additional magnetic transitions below the Curie temperature.

Figure 3(b) depicts M vs H data plotted using the Arrott formalism [27] (i.e., M^2 vs H/M) to determine the T_C of MnPtGa. The isothermal measurement which extrapolates to the origin in this type of plot is taken as the T_C. The obtained T_C of 236 K agrees reasonably well with that reported by Buschow *et al.* [25] (220 K), especially considering the variability in different T_C determination techniques.

Figure 3(c) shows representative $M(H)$ curves measured at several temperatures below T_C. The 300 K $M(H)$ is linear, showing no additional ordering in this field range, and isotherms below the ordering temperature show ferromagnet-like magnetic saturation. Magnetic hysteresis is not seen at 215 K, but at 4 K an open hysteresis loop with a coercive field of $\mu_0 H_C = 120$ mT is observed. This magnetic hysteresis is consistent with the large low-temperature irreversibility seen between the ZFC and the FC $M(T)$. The saturated moment increases as the temperature is decreased, reaching a maximum $M_{\text{sat}} = 2.63\mu_B$ at 4 and 1.8 T. This is somewhat smaller than the $M_{\text{sat}} = 3.15\mu_B$ found in a previous study [7], however, it is significantly lower than the DFT-calculated ferromagnetic moment of 3.58 μ_B, a second indicator that there may be ordering beyond simple collinear ferromagnetism at low temperatures.

Figure 4 shows a characterization of the magnetocaloric magnetic entropy change (ΔS_M) at different temperatures and fields. ΔS_M is the entropy change yielded by isothermal application of an external magnetic field, $\Delta S_M(H, T)$. The peak value of ΔS_M will occur near the Curie temperature where the magnetization changes quickly as a function of the temperature, as seen in Eq. (1). Figure 4(a) shows smoothed $M(T)$ data at several magnetic field strengths. These curves were differentiated with respect to temperature and integrated with respect to field, resulting in the $\Delta S_M(T, H)$ shown in Fig. 4(b).

For a field change of $\Delta H = 5$ T the peak ΔS_M is $-1.9\,\text{J kg}^{-1}\,\text{K}^{-1}$. This value is smaller than expected based on the Σ_M prediction. FeB, which has a similar Σ_M (2.2% for

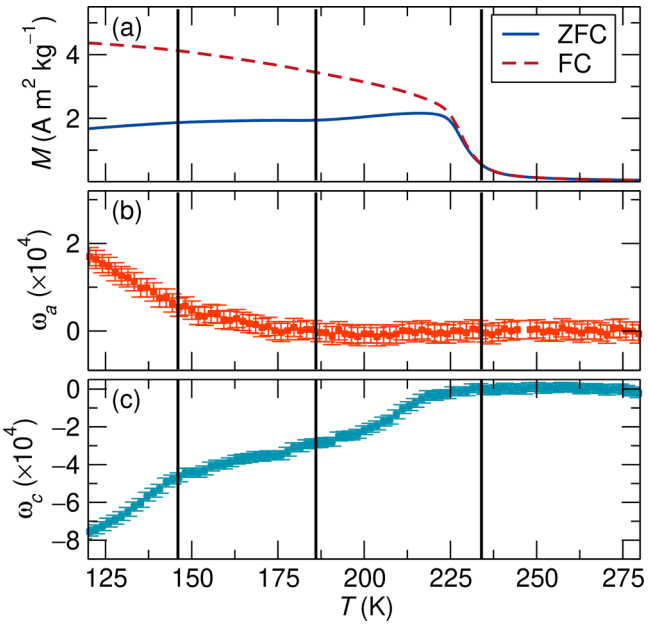

FIG. 5. (a) Temperature–dependent ZFC and FC magnetizations measured under an $H = 20$ mT field are compared to (b) magnetostriction along the a axis, ω_a, and (c) magnetostriction along the c axis, ω_c, to emphasize structural changes coincident with magnetic phenomena.

FeB *vs.* 2.4% MnPtGa), has a larger gravimetric peak ΔS_M, -3.2 J kg^{-1} K^{-1} [11]. Other materials in Ref. [9] with similar Σ_M values have even larger ΔS_M. However, this analysis is affected by the presence of heavy Pt, which makes up 61% of MnPtGa by mass. The volumetric ΔS_M of MnPtGa is -22.3 mJ cm^{-3} K^{-1} [Fig. 4(c), right axis], comparable to the volumetric ΔS_M of FeB (-22.4 mJ cm^{-3} K^{-1}). Furthermore, a deviation of the magnetic structure from the previously assumed collinear ferromagnetic ground state may impact the validity of the Σ_M prediction, and the lower than expected magnetocaloric performance is an indicator of more complex magnetic ordering beyond collinear ferromagnetism.

In order to further investigate the coupling of magnetism and crystal structure in this structure, we performed temperature-dependent synchrotron diffraction experiments through the magnetic transition temperature. The unit cell parameters a and c were obtained from sequential Rietveld refinement and indicate spontaneous volume magnetostriction below T_C. The unit cell parameters and unit cell volume show a change in slope at $T_C = 236$ K (Supplemental Material, Figs. S6 and S7), indicating spontaneous volume magnetostriction [28,29], which can be quantified as $\omega = (a - a_p)/a_p$. Here, a is the experimentally observed a (or c) unit cell parameter at a given temperature, and the "paramagnetic" unit cell parameter a_p is approximated by linear extrapolation of the lattice parameter as a function of the temperature above the Curie temperature to temperatures below the Curie temperature. The resultant plots of temperature-dependent ω_a and ω_c compared to $M(T)$ are shown in Fig. 5. In this case, it can clearly be seen that the effect of magnetic ordering near $T_C = 236$ K is to decrease c, indicating negative spontaneous magnetostriction at T_C, while there is negligible magnetostriction in the a direction. There is then another change in slope of the c lattice parameter at $T = 186$, coinciding with an observed kink in the zero-field-cooled $M(T)$, indicating that the magnitude of magnetostructural coupling decreases below this point. Then, at 146 K, coinciding with a kink seen in the field-cooled $M(T)$, the c lattice parameter slope once again increases, and additionally, the onset of magnetostriction in the a lattice parameter is observed. From these results, we can clearly see that the observed magnetic transitions in MnPtGa are coupled to changes in the crystal structure.

Overall, the spontaneous volume magnetostriction (Figs. S6 and S7 of the Supplemental Material) is negative in MnPtGa, which is somewhat unusual in Mn-based intermetallics. Often, magnetic ordering leads to expanded volume in such systems, as magnetism favors localization of the itinerant electrons [11,30–36]. However, in a few cases negative volume magnetostriction has been reported, such as in the antiferromagnets MnO and MnS [37] and the magnetocalorics Mn_5Ge_3 [38] and $Mn_{1+x}Sb$ [39]. In these cases, the volume dependence of the magnetic exchange energy is implicated as the dominant driver of the magnetostructural interaction. This volume dependence may in principle be either positive or negative, with a negative dependence indicating that the magnetic exchange energy decreases as the atoms move apart, leading to a negative contribution to the magnetostriction as is often seen in lanthanide-based magnets [40].

C. Magnetic structure

In order to determine the temperature evolution of the magnetic structure of MnPtGa, NPD data were collected at various temperatures (Fig. 6) between 300 and 10 K. At 300 K, only peaks and intensity corresponding to the nuclear Ni_2In ($P6_3/mmc$) structure are observed. At 200 K, below T_C but above the first kink in the temperature-dependent magnetization, additional intensity is observed in some of the low-Q nuclear peaks, but no new peaks arise. This is consistent with a ferromagnetic structure with a moment of approximately 3 μ_B on each Mn, pointing in the c direction [Fig. 8(a)].

At around 186 K, we see a change in slope in the temperature-dependent magnetization. Below this slope change, at 150 K, additional neutron diffraction peaks are observed [Fig. 6(c)], corresponding to the structurally forbidden (001) and (211) indexes of the hexagonal nuclear unit cell. Because both of these peaks correspond to an integer index within the primitive nuclear unit cell, we can conclude that the magnetic structure has a k vector of (0,0,0) (i.e., the nuclear and magnetic unit cell are the same). We next used the ISODISTORT software to generate the possible irreducible representations (irreps) and order parameter directions (OPDs) for magnetic structures with moments at the Mn site consistent with this k vector. We find an excellent fit to the data with the mΓ_5^+ irrep and P_2 OPD, giving the canted magnetic structure shown in Fig. 8(b) with magnetic space group $Cm'c'm$. In this structure, only two magnetic modes are active: one which gives ferromagnetic moment components in the c direction and one which gives antiferromagnetic moment components pointed in the a direction and alternating direction along the c axis. The resulting structure may be thought

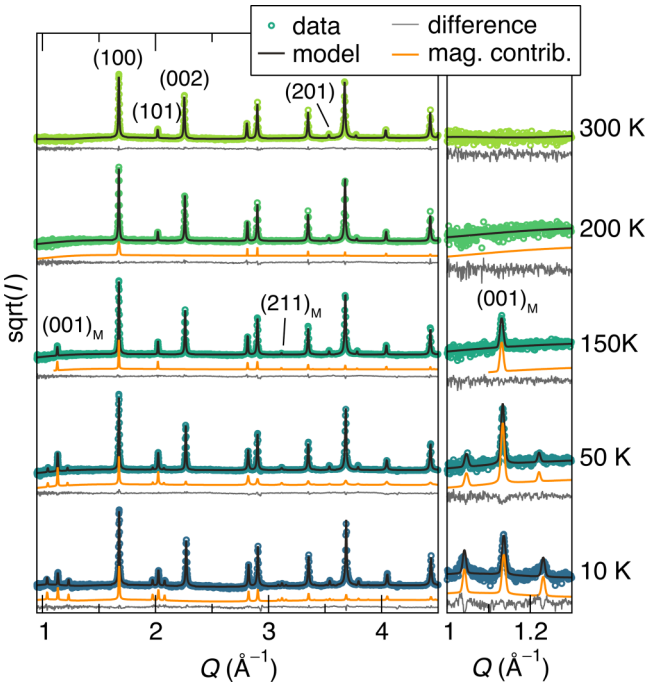

FIG. 6. Magnetic Rietveld refinements of POWGEN data collected using center wavelength 2.665 Å at 300, 200, 150, 50, and 10 K. The 300 K pattern contains only the nuclear intensity, the 200 K pattern shows the addition of additional magnetic intensity on the nuclear peaks, and the 150 K and lower patterns show new principal peaks and magnetic satellites. The right column shows a closer view of the (001) magnetic peak and its satellites.

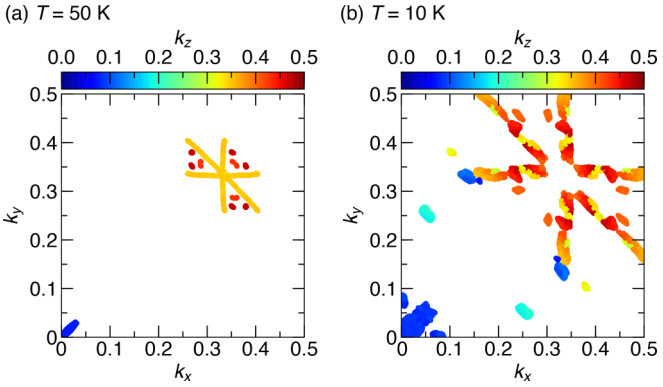

FIG. 7. Space of plausible k vectors consistent with (a) the two sets of magnetic satellites observed at 50 K and (b) the four sets at 10 K. Each possible k vector with a K-SEARCH R factor less than 0.4 (for 50 K) or 3 (for 10 K) is displayed as a point. These maps reveal that the possible k vectors at both temperatures cluster in high-symmetry lines and points around (1/3, 1/3, 1/3) and (0, 0, z).

of as a canting from the ferromagnetic structure in alternate directions or as a heavily canted antiferromagnet with moment switching along the c axis. This magnetic structure is similar to that reported for MnPdGa [41] and MnCoSn [42,43] at low temperatures, although in MnPdGa the antiferromagnetic mode is dominant and the structure is closer to an antiferromagnet. In MnPdGa, the moments are canted 56° from the c axis [41], in MnCoSn they are canted 34(4)° [43], and in MnPtGa they are canted 24(1)°. This structure results in a net ferromagnetic moment of 2.44(6)μ_B along the c axis in MnPtGa.

Near 140 K, we see an additional slope change in the temperature-dependent magnetization. Below this kink, at 50 K, we see satellite peaks emerge in the NPD data about some of the nuclear and magnetic peaks. At 50 K, satellites are visible about the (001) magnetic peak and (101) nuclear/magnetic peak (Fig. 6). At 10 K, these satellites grow stronger and additional satellites about the (211) magnetic peak and (201) nuclear/magnetic peak can be resolved. The satellites indicate the presence of a modulated magnetic structure, with an additional k vector to the (0,0,0) k vector identified at 150 K. In order to determine the new magnetic unit cell, we used the program K-SEARCH. This program searches for possible supercells of a given nuclear unit cell that can describe a set of observed satellite positions. Upon searching for commensurate k vectors, we identified that all

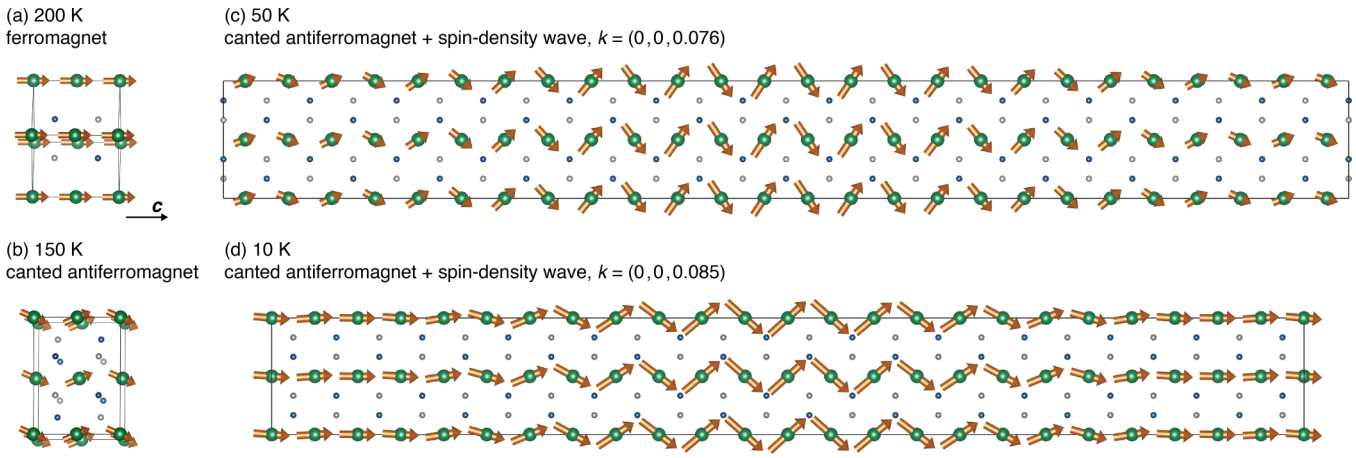

FIG. 8. Evolution of the magnetic structure of MnPtGa from neutron powder diffraction. It transitions from (a) a ferromagnet at 200 K to (b) a canted antiferromagnet at 150 K to (c, d) a canted antiferromagnet plus spin density wave that increases in amplitude upon cooling to 10 K. In (c) and (d), the unit cells drawn are commensurate unit cells used to approximate the incommensurate magnetic structures.

TABLE I. Crystallographic data for MnPtGa.

	Temperature				
	10 K	50 K	150 K	200 K	300 K
Space group (no.)	$C2'/m'$ (12.62)[a]	$Amm'2'$ (38.190)[a]	$Cm'c'm$ (63.462)	$Cm'c'm$ (63.462)	$P6_3/mmc$ (194)
a (Å)	7.4894(3)	72.011(8)	4.3298(4)	4.3308(5)	4.3304(2)
b (Å)	4.3240(1)	4.3281(5)	7.4994(8)	7.5011(8)	—
c (Å)	66.380(4)	7.4966(2)	5.5538(5)	5.5610(1)	5.5726(6)
$\alpha,\ \beta,\ \gamma$	90, 90, 90	90, 90, 90	90, 90, 90	90, 90, 90	90, 90, 120
V (Å^3)	2150.4(4)	2336.5(6)	180.33(2)	180.65(3)	90.50(1)
Net ferromagnetic moment (μ_B)	3.1(3)	2.0(9)	2.5(6)	3.1(6)	—
Local moment magnitude (μ_B)	3.4–4.5	2.2–3.7	2.7	3.1	—
GOF (R_{wp}/R_{exp})	3.341, 2.702[b]	3.989	3.502	2.695	2.629, 2.936[b]

[a]Space groups and lattice parameters provided for 10 and 50 K are for the commensurate unit cells used to approximate the incommensurate magnetic structure.
[b]GOF for data with center wavelength 2.665 Å and 0.8-Å corefinement.

but the weakest of the 10 K satellites could be well fit using a (1/3, 1/3, 1/3) k vector, indicating a magnetic cell that is tripled along all three hexagonal axes. However, upon enumerating the possible irreps and OPDs consistent with this k vector, we were unable to satisfactorily fit the peak intensities.

We therefore proceeded to revisit the chosen k vector, expanding the search to incommensurate vectors. This search, which is equivalent to indexing a powder pattern with an arbitrary triclinic cell, yielded tens of thousands of possible k vectors spanning different areas of k space, many with approximately equal R factors (a goodness-of-fit indicator calculated by summing d-space deviations of the observed satellites from predicted satellite positions). In order to understand these results, we plotted them in k space, as shown in Fig. 7. We found that at both 10 and 50 K, plausible k vectors often clustered around (1/3, 1/3, 1/3) and in high-symmetry lines from this position. However, additional clusters also exist around the (0,0,z) position, with $z = 0.076$ at 50 K and $z = 0.085$ at 10 K. These k vectors indicate magnetic structures with long-period (approximately 12 or 13 unit cells) incommensurate one-dimensional modulations along the c axis.

Using the (0,0,z) k vectors, a simple magnetic structure was obtained that correctly models all satellite positions and intensities in both the 10 and the 50 K patterns [Figs. 8(c) and 8(d)]. In addition to the $k = (0, 0, 0)$ modes previously identified, a second irrep becomes active: the incommensurate $m\Delta_2$ irrep with the P OPD. In order to refine the magnetic structure in TOPAS Academic, which does not support refining incommensurate structures, we approximated the periodicity using cells with the c axis set to the integer multiple of the nuclear c axis closest to $1/z$. This corresponds to 13 unit cells at 50 K and 12 unit cells at 10 K. Using these descriptions, only a single new mode (in addition to the two modes refined at 150 K) was needed to describe the patterns at both 50 and 10 K: an antiferromagnetic spin-density wave with moments oriented in the hexagonal a direction and flipping along the c axis [$m\Delta_2\ E_g(a)$]. This mode modulates the magnitude of the antiferromagnetic component of the magnetic structure in a sine wave with a period of 12 or 13 unit cells, resulting in the fascinating canted spin-density structures depicted in Figs. 8(c) and 8(d). The magnitude of this mode is relatively small at 50 K, which is why only two sets of satellites were resolvable in the diffraction data. At 10 K, this mode is stronger and four sets may be resolved. At this temperature, the moment on the Mn in the c direction is 3.1 μ_B, and the moment in the ab plane oscillates between 3 μ_B and $-3\mu_B$. The details of crystallographic data refinement are listed in Table I.

It is interesting to ask whether this incommensurate magnetic structure along the c axis also forms in the skyrmion-hosting sample of MnPtGa reported by Srivastava *et al.*, as the skyrmions themselves are incommensurate magnetic structures with very long unit cells modulating in the ab plane (in this case, wavelengths of the order of 800–1800 nm). Most skyrmion hosts that have been studied are assumed to show ferromagnetic ordering within the unit cell, which then rotates over long periods to form the interesting topological magnetic states. However, in some cases more exotic local magnetic structures have been found to interact in interesting ways with long-period skyrmionic order. For example, this occurs in the multiferroic ferrimagnet Cu_2OSeO_3[44], the ferrimagnetic antiskyrmion host $Mn_{1.4}Pt_{0.9}Pd_{0.1}Sn$ [45], compensated ferrimagnetic films of GdCo [46], and the spin-glass state of $Co_xZn_yMn_z$ [47,48]. We are not aware of any so-far-reported skyrmion hosts in which the local magnetic structure involves a shorter-period incommensurate spin wave.

We also note that solving magnetic structures from unpolarized powder diffraction data necessarily involves some ambiguity. The solutions we have presented are the highest-symmetry, simplest solutions that we found to satisfactorily reproduce the observed neutron diffraction patterns. However, more complex structures may fit the data equally well. In particular, powder diffraction cannot determine the moment orientation within the hexagonal ab plane. Furthermore, an antiferromagnetic helical mode with constant moment magnitudes rotating in the ab plane with $1/z$ period fits the satellites equivalently to the magnitude-modulated mode we have presented. However, this mode leads to a much lower-symmetry cell, and furthermore, the constructive and destructive interaction of this mode with the $k = 0$ antiferromagnetic

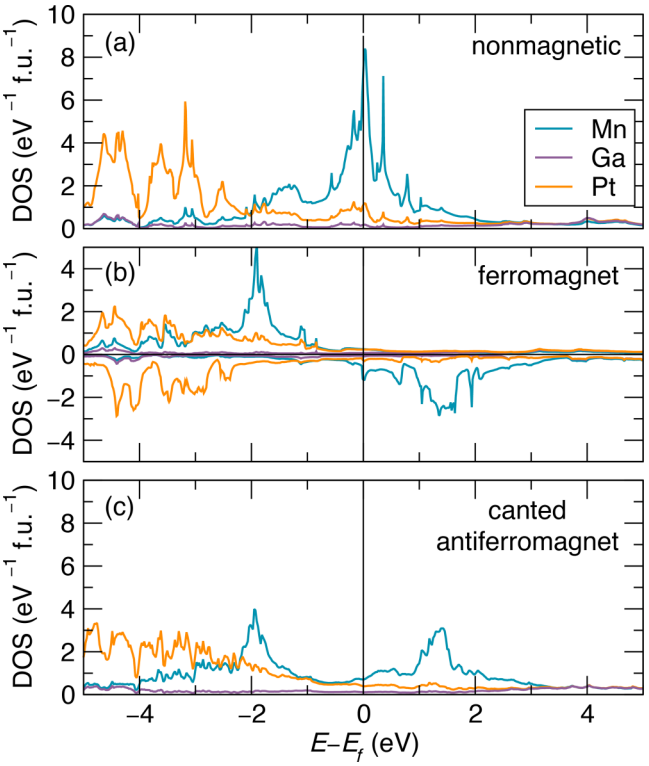

FIG. 9. Site-projected calculated density of states (DOS) diagram in (a) the non-spin-polarized state, (b) the spin-polarized state with collinear ferromagnetic order, with a small peak in the minority spin channel, and (c) the spin-polarized state with noncollinear magnetic order consistent with the solved magnetic structure.

mode causes the overall magnetic structure to show a spin-density-wave-like structure in either case. Future studies on single-crystal samples of MnPtGa, as well as an examination of the field-driven evolution of magnetic structure, could prove interesting to elucidate complexities of the magnetic and structural phase diagram and establish control over the structure and magnetic properties of this versatile material.

Figure 9 shows the site-projected calculated density of states (DOS) for MnPtGa in (a) the non-spin-polarized state and (b) the spin-polarized state with collinear ferromagnetic order (no spin-orbit coupling included) and (c) with spin-orbit coupling in the $k = 0$ structure observed in the neutron diffraction data at 150 K [Fig. 8(b)]. In the non-spin-polarized state, the Mn states form a strong peak at the Fermi level, with a total DOS at the Fermi level $N(E_F = 9.27\ \text{eV}^{-1}$ per formula unit. This peak represents an electronic instability which may be relieved by an electronic distortion into a spin-polarized state. The Stoner criterion states that a system is likely to become ferromagnetic if the product of the exchange energy and the nonmagnetic density of states at the Fermi level is greater than unity [$I \cdot N(E_F) > 1$]. For a typical value of the Mn exchange energy (I), 0.4 eV [49], MnPtGa easily satisfies this criterion.

When a spin-polarized ferromagnetic calculation is performed [Fig. 9(b)], a Mn moment of $3.58\mu_B$ is found to form, with no substantial moment on the Pt and Ga ions. This spin polarization greatly reduces the DOS at the Fermi level [Fig. 9(b)]. Interestingly, however, a small peak in the

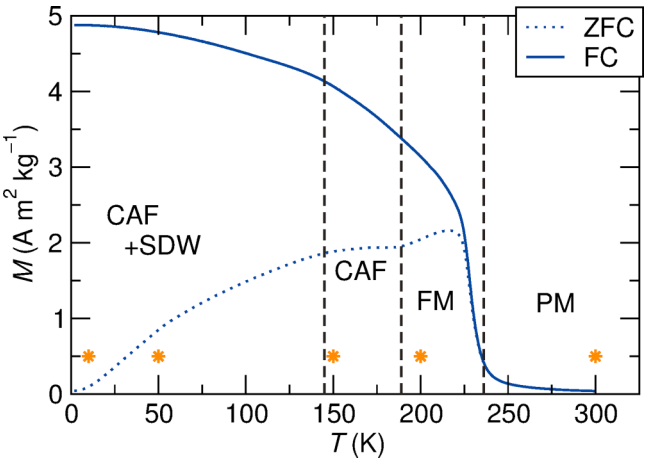

FIG. 10. The proposed phase diagram of MnPtGa from room temperature to 2 K includes a paramagnetic (PM) region to 236 K, collinear ferromagnetism (FM) from 236 to 175 K, a canted antiferromagnet (CAF) from 175 to 148 K, and a CAF plus spin-density wave (SDW) from 148 to 2 K. Vertical lines indicate kinks in the M vs T data and asterisks indicate temperatures at which neutron diffraction data were obtained and analyzed.

minority spin channel remains. This leads to a total DOS at the Fermi level of $2.46\,\text{eV}^{-1}$ per formula unit, which still gives $I \cdot N(E_F) = 0.98$. This peak at the Fermi level is not relieved by the inclusion of spin-orbit coupling in the ferromagnetic calculation and the orientation of the moments in either the [001] or the [100] direction (Supplemental Material, Fig. S8). Therefore, it appears that a ferromagnetic spin structure can stabilize the electronic structure with respect to the nonmagnetic state but that there is still an opportunity for subsequent symmetry-lowering magnetic transitions to lower the energy even further. Indeed, when a spin-polarized calculation is performed that is consistent with the canted antiferromagnetic state, the peak at the Fermi level is eliminated [$I \cdot N(E_F) = 0.57$] and the overall energy of the calculation is decreased. This stabilization explains why MnPtGa transitions from the ferromagnetic to the canted antiferromagnetic state as it is cooled below 200 K. We have not, however, attempted calculations on the incommensurate magnetic states we observed at lower temperatures in the neutron diffraction.

IV. CONCLUSION

The intermetallic magnet MnPtGa has been prepared and characterized, following the suggestion that it may show strong magnetostructural coupling and therefore substantial magnetocaloric effects. A small but negative spontaneous volume magnetostriction has been found, associated with contraction in the interlayer direction upon the onset of magnetic order. The magnetic entropy change associated with the magnetic ordering transition is $-1.99\,\text{J}\,\text{kg}^{-1}\,\text{K}^{-1}$ for a 5-T applied field. Motivated by the lower-than-expected magnetocaloric effect and anomalies in magnetization measurements, the magnetic structure was examined using neutron powder diffraction and found to evolve as a function of (decreasing) temperature from a ferromagnet, to a canted

TABLE II. Results of DFT calculations on MnPtGa with different magnetic structures.

	$E - E_{\min}$ (meV f.u.$^{-1}$)	Local moment (μ_B)	Net moment (μ_B f.u.$^{-1}$)
Nonmagnetic	1476		
Ferromagnetic[a]	12.9	3.59	3.57
Canted[b]	0	3.57	3.28

[a]Moments oriented along the hexagonal c axis.
[b]Structure shown in Fig. 8(b).

antiferromagnet, and, finally, to a canted antiferromagnet with a spin-density wave in the c direction at 10 K (Fig. 10). These deviations from the previously assumed collinear ferromagnetic structure appear to be in agreement with magnetic measurements, density functional theory calculations (Table II), and the measured magnetic entropy change.

ACKNOWLEDGMENTS

This work was supported by the Materials Research Science and Engineering Center (MRSEC) at UC Santa Barbara through NSF Grant No. DMR-1720256 (IRG-1). The use of the shared facilities of the MRSEC is gratefully acknowledged; the UCSB MRSEC is a member of the Materials Research Facilities Network (www.mrfn.org). J.D.B. acknowledges support from the NSF Graduate Research Fellowship Program under Grant No. DGE-1650114. Use of the Advanced Photon Source at Argonne National Laboratory was supported by the U.S. Department of Energy, Office of Science, Office of Basic Energy Sciences, under Contract No. DE-AC02-06CH11357. A portion of this research conducted at Oak Ridge National Laboratory's Spallation Neutron Source was sponsored by the Scientific User Facilities Division, Office of Basic Energy Sciences, U.S. Department of Energy.

[1] E. P. Wohlfarth, Adv. Phys. **8**, 87 (1959).
[2] P. Kumar, A. Kashyap, B. Balamurugan, J. E. Shield, D. J. Sellmyer, and R. Skomski, J. Phys.: Condens. Matter **26**, 064209 (2014).
[3] A. Kussmann and G. Von Rittberg, Z. Metallkd. **41**, 470 (1950).
[4] S. Khmelevskyi, I. Turek, and P. Mohn, Phys. Rev. Lett. **91**, 037201 (2003).
[5] L. H. Lewis, C. H. Marrows, and S. Langridge, J. Phys. D: Appl. Phys. **49**, 323002 (2016).
[6] M. G. Vergniory, L. Elcoro, F. Orlandi, B. Balke, Y.-H. Chan, J. Nuss, A. P. Schnyder, and L. M. Schoop, Eur. Phys. J. B **91**, 213 (2018).
[7] K. H. J. Buschow, Phys. Status Solidi **76**, 615 (1983).
[8] A. K. Srivastava, P. Devi, A. K. Sharma, T. Ma, H. Deniz, H. L. Meyerheim, C. Felser, and S. S. P. Parkin, Adv. Mater. **32**, 1904327 (2019).
[9] J. D. Bocarsly, E. E. Levin, C. A. C. Garcia, K. Schwennicke, S. D. Wilson, and R. Seshadri, Chem. Mater. **29**, 1613 (2017).
[10] C. A. C. Garcia, J. D. Bocarsly, and R. Seshadri, Phys. Rev. Materials **4**, 024402 (2020).
[11] J. D. Bocarsly, E. E. Levin, S. A. Humphrey, T. Faske, W. Donner, S. D. Wilson, and R. Seshadri, Chem. Mater. **31**, 4873 (2019).
[12] A. Huq, M. Kirkham, P. F. Peterson, J. P. Hodges, P. S. Whitfield, K. Page, T. Hugle, E. B. Iverson, A. Parizzi, and G. Rennich, J. Appl. Crystallogr. **52**, 1189 (2019).
[13] J. Rodríguez-Carvajal, Physica B **192**, 55 (1993).
[14] B. J. Campbell, H. T. Stokes, D. E. Tanner, and D. M. Hatch, J. Appl. Crystallogr. **39**, 607 (2006).
[15] H. T. Stokes, D. M. Hatch, and B. J. Campbell, ISODISTORT, Isotropy Software Suite; iso.byu.edu.
[16] A. A. Coelho, J. Appl. Crystallogr. **51**, 210 (2018).
[17] K. Momma and F. Izumi, J. Appl. Crystallogr. **44**, 1272 (2011).
[18] B. H. Toby and R. B. Von Dreele, J. Appl. Crystallogr. **46**, 544 (2013).
[19] J. J. Stickel, Comput. Chem. Eng. **34**, 467 (2010).
[20] J. D. Bocarsly, R. F. Need, R. Seshadri, and S. D. Wilson, Phys. Rev. B **97**, 100404(R) (2018).
[21] G. Kresse and J. Furthmüller, Phys. Rev. B **54**, 11169 (1996).
[22] P. E. Blöchl, Phys. Rev. B **50**, 17953 (1994).
[23] G. Kresse and D. Joubert, Phys. Rev. B **59**, 1758 (1999).
[24] J. P. Perdew, K. Burke, and M. Ernzerhof, Phys. Rev. Lett. **77**, 3865 (1996).
[25] K. H. J. Buschow and D. B. de Mooij, J. Less-Common Met. **99**, 125 (1984).
[26] See Supplemental Material at http://link.aps.org/supplemental/10.1103/PhysRevMaterials.4.044405 for x-ray fluorescence data, additional synchrotron X-ray and neutron diffraction data Rietveld refinements, microscopy image, and additional densities of states diagram.
[27] A. Arrott, Phys. Rev. **108**, 1394 (1957).
[28] J. Kusz, S. Juszczyk, and J. Warczewski, J. Appl. Crystallogr. **21**, 898 (1988).
[29] A. Bombik, H. Bohm, J. Kusz, and A. W. Pacyna, J. Magn. Magn. Mater. **234**, 443 (2001).
[30] E. Wohlfarth, Physica B+C **91**, 305 (1977).
[31] T. Moriya and K. Usami, Solid State Commun. **34**, 95 (1980).
[32] M. Shiga, H. Wada, and Y. Nakamura, J. Magn. Magn. Mater. **31–34**, 119 (1983).
[33] V. A. Chernenko, L. Wee, P. G. McCormick, and R. Street, J. Appl. Phys. **85**, 7833 (1999).
[34] A. M. Kadomtseva, Y. F. Popov, G. P. Vorob'ev, K. I. Kamilov, V. Y. Ivanov, A. A. Mukhin, and A. M. Balbashov, Phys. Solid State **42**, 1110 (2000).
[35] R. Huang, Y. Liu, W. Fan, J. Tan, F. Xiao, L. Qian, and L. Li, J. Am. Chem. Soc. **135**, 11469 (2013).
[36] F. Hu, F. Shen, J. Hao, Y. Liu, J. Wang, J. Sun, and B. Shen, Front. Chem. **6**, 1 (2018).
[37] B. Morosin, Phys. Rev. B **1**, 236 (1970).
[38] H. Ido, T. Suzuki, and T. Kaneko, J. Phys. Soc. Jpn. **29**, 1490 (1970).
[39] J. A. Cooley, M. K. Horton, E. E. Levin, S. H. Lapidus, K. A. Persson, and R. Seshadri, Chem. Mater. **32**, 1243 (2020).
[40] A. Lindbaum and M. Rotter, in *Handbook of Magnetic Materials*, *Vol. 14*, 1st ed., edited by K. H. J. Buschow (North-Holland, Amsterdam, 2002), pp. 307–362.

[41] H. Shiraishi, T. Hori, N. Ohkubo, K. Ohoyama, and Y. Yamaguchi, J. Appl. Phys. **93**, 6996 (2003).
[42] W. Baźla, A. Szytuła, and W. Zajac, Solid State Commun. **38**, 875 (1981).
[43] H. Shiraishi, T. Hori, N. Ohkubo, and K. Ohoyama, Physica B **384**, 319 (2006).
[44] S. Seki, X. Z. Yu, S. Ishiwata, and Y. Tokura, Science **336**, 198 (2012).
[45] A. K. Nayak, V. Kumar, T. Ma, P. Werner, E. Pippel, R. Sahoo, F. Damay, U. K. Rößler, C. Felser, and S. S. P. Parkin, Nature **548**, 561 (2017).
[46] L. Caretta, F. Büttner, K. Ueda, B. Pfau, C. M. Günther, P. Hessing, A. Churikova, C. Klose, M. Schneider, D. Engel, C. Marcus, D. Bono, K. Bagschik, S. Eisebitt, and G. S. D. Beach, Nat. Nanotechnol. **13**, 1154 (2018).
[47] K. Karube, J. S. White, D. Morikawa, C. D. Dewhurst, R. Cubitt, A. Kikkawa, X. Yu, Y. Tokunaga, T. Arima, H. M. Rønnow, Y. Tokura, and Y. Taguchi, Sci. Adv. **4**, eaar7043 (2018).
[48] J. D. Bocarsly, C. Heikes, C. M. Brown, S. D. Wilson, and R. Seshadri, Phys. Rev. Materials **3**, 014402 (2019).
[49] J. F. Janak, Phys. Rev. B **16**, 255 (1977).